Title

The Sadovskii vortex in strain

Authors

Freilich, Daniel V

Smith, Stefan G Llewellyn

Publication Date

2017-08-25

DOI

10.1017/jfm.2017.401

Peer reviewed

The Sadovskii vortex in strain

Daniel V. Freilich[1] and Stefan G. Llewellyn Smith[1]†

[1]Department of Mechanical and Aerospace Engineering, Jacobs School of Engineering, UCSD, 9500 Gilman Drive, La Jolla, CA 92093-0411, USA

(Received xx; revised xx; accepted xx)

The point vortex is the simplest model of a two-dimensional vortex with non-zero circulation. The limitations introduced by its lack of core structure have been remedied by using desingularizations such as vortex patches and vortex sheets. We investigate steady states of the Sadovskii vortex in strain, a canonical model for a vortex in a general flow. The Sadovskii vortex is a uniform patch of vorticity surrounded by a vortex sheet. We recover previously known limiting cases of the vortex patch and hollow vortex, and examine the bifurcations away from these families. The result is a solution manifold spanned by two parameters. The addition of the vortex sheet to the vortex patch solutions immediately leads to splits in the solution manifold at certain bifurcation points. The more circular elliptical family remains attached to the family with a single pinch-off, and this family extends all the way to the simpler solution branch for the pure vortex sheet solutions. More elongated families below this one also split at bifurcation points, but these families do not exist in the vortex sheet limit.

1. Introduction

A long-standing problem in vortex dynamics is the construction of equilibrium vortex shapes. Given the complexity of the problem, the two-dimensional case has been the subject of particular attention, given its relevance to situations with weak variations in one direction, for example because of stratification. The two-dimensional flow due to a point vortex in an otherwise irrotational flow is described by the complex potential

$$w = \phi + \mathrm{i}\psi = \frac{\Gamma}{2\pi\mathrm{i}} \ln z, \tag{1.1}$$

where Γ is the circulation of the vortex and $z = x + \mathrm{i}y$. While the point vortex is a useful model for the behaviour of the fluid outside the vortex (where the distance from the vortex is much larger than the core size), it is less useful for modeling the behaviour and dynamics of the vortex core and the motion of the fluid close to the vortex. This has motivated research into desingularizations of the point vortex, in particular using vortex sheets and vortex patches.

A vortex sheet is a discontinuity in the velocity of the fluid, and the strength of the sheet is related to the jump in velocity tangential to the sheet as one crosses from one side to the other. This configuration is a delta function of vorticity in the direction normal to the sheet. A closed vortex sheet is one possible desingularization of a point vortex. It can also be viewed as a bubble with circulation. Far from the vortex sheet, the flow resembles that due to a point vortex as in (1.1).

Previous work on equilibrium vortex sheets has focused on hollow vortices, for which the density vanishes inside the vortex. Previous research on hollow vortices examined equilibrium solutions such as pairs (Pocklington 1895; Moore & Pullin 1987; Leppington

† Email address for correspondence: sgls@ucsd.edu

2006) or rows (Baker *et al.* 1976; Ardalan *et al.* 1995). More recently, Llewellyn Smith & Crowdy (2012) investigated both the shape and stability of a single steady hollow vortex in a straining field, and gave a description of its stability. Other work has looked at the von Kármán street of hollow vortices (Crowdy & Green 2011) and at hollow vortices in a channel (Green 2015).

A vortex patch is an area of fluid containing nonzero vorticity. As with the vortex sheet, far from the patch, the flow looks like the flow due to a point vortex with the same circulation. Here, we focus only on patches of uniform vorticity. In this case, the problem can be reduced from the underlying partial differential equations to contour dynamics (Zabusky *et al.* 1979), which requires only knowledge the boundary of the vortex patches. This method was also used to calculate new vortex patch configurations termed V-states. Deem & Zabusky (1978) used this method to find new rotating and translating states of vortex patches, besides the known Kirchhoff vortices (Lamb 1932). It was used for both individual vortex patches and to look at the interactions between multiple vortex patches.

Moore & Saffman (1971) calculated steady elliptical states of a vortex patch in a straining field. This work also included a stability analysis that found those ellipses that were neutrally stable and could be the starting states for bifurcated solutions of different shapes. Kamm (1987) used Schwarz functions to investigate non-elliptical vortex patches in strain. The bifurcation points of the family of elliptical solutions matched those predicted by Moore & Saffman (1971), and all the non-elliptical vortices in strain were found to be unstable. The three-dimensional stability was investigated in Robinson & Saffman (1984) and Miyazaki *et al.* (1995). Kida (1981) obtained solutions for vortex patches in uniform shear.

The Sadovskii vortex† is a combination of the previously discussed vortex desingularizations: it is a vortex patch surrounded by a vortex sheet. This type of flow was previously investigated in works on bluff body wakes, including in Chernyshenko (1998). The Prandtl–Batchelor theorem shows that the vorticity inside a closed streamline tends to a constant value in the high Reynolds number limit (Batchelor 1956*a*). Batchelor (1956*b*) argued that in bluff body wakes, the region of constant vorticity is bounded by a jump in tangential velocity (a vortex sheet), motivating further work, including that of Sadovskii (1971), who investigated a flow in which there is a jump in the Bernoulli constant on the boundary of the vortex and the vorticity is organized into two patches of equal and opposite vorticity. Outside this region, the flow is incompressible and irrotational.

Other related works are Moore *et al.* (1988); Saffman & Tanveer (1984). The latter obtained the Prandtl-Batchelor flow past a body with a forward facing flap. This leads to an area of constant vorticity inside this angled section, and irrotational flow outside a streamline going from one edge of the plate to the other which is a vortex sheet, as manifested by a jump in the Bernoulli constant. This problem was solved using conformal mappings for the inside and outside of the vortex, and then finding the correspondence between the boundary points in each mapping. Bunyakin *et al.* (1996), Bunyakin *et al.* (1998), and Chernyshenko *et al.* (2003) investigated flows with vortex patches trapped in airfoil cavities.

Our goal here is to generalize the hollow vortex in strain of Llewellyn Smith & Crowdy (2012) and the elliptical vortex patches in strain of Moore & Saffman (1971)

† Such flows have been called "Batchelor flows" in the literature, but we avoid the expression "Batchelor vortex" to minimise confusion with the Batchelor vortex, which refers to a three-dimensional vortex with axial flow.

by computing the Sadovskii vortex in strain. There will now be two governing non-dimensional parameters and the solutions will form a manifold in this parameter space. The relation between the known solutions is particularly interesting, because the Moore–Saffman vortices have a known bifurcation structure, while no such structure exists for the hollow vortex in strain. The case of a vortex in strain is a canonical one, since locally any flow looks like a strain, so this flow gives the local response of a vortex in a large-scale and more general complicated flow.

This paper is structured as follows. Section 2 describes the problem and boundary conditions. Sections 3 and 4 use numerical continuation to recalculate solutions to the patch and sheet cases, including families of bifurcating solutions. Section 5 presents solutions to the Sadovskii vortex in strain, and discusses the changes in the bifurcation diagram and vortex shapes as the contributions from interior and boundary circulation change. Section 6 presents conclusions. A discussion of the numerical method is given in the Appendix.

2. Formulation

The Sadovskii vortex is a patch of fluid with uniform vorticity surrounded by a vortex sheet. Inside the vortex, we require constant vorticity ω, so we solve Poisson's equation

$$\nabla^2\psi = -\omega, \tag{2.1}$$

where ψ is the streamfunction with

$$u = \frac{\partial\psi}{\partial y}, \qquad v = -\frac{\partial\psi}{\partial x}. \tag{2.2}$$

Outside the vortex, the flow is irrotational, so we solve Laplace's equation

$$\nabla^2\psi = 0. \tag{2.3}$$

We require that far from the vortex, the stream function correspond to a straining field along with circulation, so that

$$\psi \sim \gamma\left(x^2 - y^2\right) - \frac{\Gamma}{2\pi}\ln|z| \quad \text{as} \quad |z| \to \infty, \tag{2.4}$$

where γ gives the strength of the strain.

We require the boundary of the vortex to be a streamline, which means that

$$\psi = \text{constant} \tag{2.5}$$

on the boundary of the vortex. Since we can define the streamfunction ψ up to a constant, without loss of generality we set $\psi = 0$ on the boundary. This condition can also be written in terms of the velocity as

$$\mathbf{u}\cdot\hat{\mathbf{n}} = 0, \tag{2.6}$$

where $\mathbf{u} = (u, v)$ is the velocity, and $\hat{\mathbf{n}}$ is the normal vector to the vortex boundary.

The second condition is the dynamic condition, which we also call the pressure condition or Bernoulli condition. As in Saffman (1992), the Bernoulli condition for steady, inviscid, incompressible flows in regions with constant vorticity and no body forces is

$$\frac{\rho}{2}|\mathbf{u}|^2 - \rho\omega\psi + p = \text{constant}. \tag{2.7}$$

In irrotational regions (in this paper, everywhere outside the vortex), $\omega = 0$ and this

condition is the usual

$$\frac{\rho}{2}|\mathbf{u}|^2 + p = \text{constant}. \tag{2.8}$$

The pressure must be continuous across the boundary of the vortex since we are neglecting surface tension. We have taken $\psi = 0$ on the boundary of the vortex, so

$$\frac{1}{2}\rho_{out}|\mathbf{u}_{out}|^2 - \frac{1}{2}\rho_{in}|\mathbf{u}_{in}|^2 = Q, \tag{2.9}$$

where ρ_{in} is the density inside the vortex core, ρ_{out} is the density outside the vortex, and Q is the difference in Bernoulli constant between the inside and outside of the vortex. In cases with $\rho_{in} = \rho_{out}$, if $Q = 0$ the velocity is continuous at the vortex boundary and there is no vortex sheet: this is the vortex patch. If $Q \neq 0$, there is a jump in the Bernoulli constant and velocity at the boundary, which is a vortex sheet. When $\rho_{in} \neq \rho_{out}$, it is possible to have $Q = 0$ and a vortex sheet, since a vortex sheet exists wherever $|\mathbf{u}_{out}| \neq |\mathbf{u}_{in}|$. The case in which the vorticity is zero, $\omega = 0$, is the vortex sheet. We consider only the case when the densities are equal or when the second term in (2.9) vanishes, which occurs when there is no vortex patch (including the special case of the hollow vortex with $\rho_{in} = 0$). Our method can still be used in the case with different densities, but this introduces a new parameter without much new insight.

3. Vortex patch

3.1. *Elliptical solutions*

The velocity field due to a vortex patch is continuous at the vortex boundary, so for equal densities we have $\rho_{in} = \rho_{out}$ and $Q = 0$ in (2.9). Moore & Saffman (1971) showed that elliptical vortex patches are steady solutions in a straining field. Solutions exist when

$$\frac{e}{\omega} = \frac{\theta(\theta - 1)}{(\theta^2 + 1)(\theta + 1)}, \tag{3.1}$$

where $e = 2\gamma$ is twice the value of the strain rate and $\theta = a/b > 1$ is the ratio of the ellipse's semi-major to semi-minor axes. The relation (3.1) links the shape of the ellipse to the nondimensional ratio of strain to vorticity. In what follows we will use a different quantity that characterizes the shape of the ellipse, namely the ratio of the square root of area to perimeter, since it exists for arbitrary shapes. This is not a unique way of describing the shape (except for ellipses), but measures how far from circular the shape is.

Along with computing this family of elliptical vortices in other flow fields such as shear, Moore and Saffman also carried out a stability analysis and found that the growth rate of the azimuthal mode m is

$$\sigma^2 = -\frac{\omega^2}{4}\left(\frac{2m\theta}{\theta^2 + 1} - 1\right)^2 - \frac{1}{4}\left(\frac{\theta - 1}{\theta + 1}\right)^{2m}. \tag{3.2}$$

The points where $\sigma = 0$ gives the locations of bifurcations from the elliptical family. Kamm (1987) used a continuation method to search for bifurcations at these points. The point for $m = 2$ is the fold point in the family, at which the stability of the ellipse changes from stable to unstable and the ellipses become more eccentric for the same value of e/ω. Kamm (1987) found the initial shapes of the next three bifurcating families, but was unable to compute them completely because of limitations of his continuation method. Families that bifurcate at even values of m are symmetric about both the x- and y-axes, while those that bifurcate at odd values of m were found to be symmetric only about the x-axis.

3.2. *Procedure*

We follow the approach given in the Appendix. The complex velocity due to the vortex patch can be calculated as a boundary integral, as shown in Luzzatto-Fegiz & Williamson (2011):

$$\mathbf{u}_{\text{patch}}(\mathbf{x}) = \frac{\omega}{2\pi} \oint \frac{\mathbf{x}-\mathbf{X}}{|\mathbf{x}-\mathbf{X}|^2}(\mathbf{x}-\mathbf{X}) \cdot \frac{\mathrm{d}\mathbf{X}}{\mathrm{d}\tilde{s}}\, \mathrm{d}\tilde{s}, \tag{3.3}$$

where $\tilde{s}$ is a parameterization of the boundary (not necessarily arc length), $\mathbf{u}_{\text{patch}}$ is the velocity due to the patch, and the total velocity is

$$\mathbf{u}(\mathbf{x}) = \mathbf{u}_{\text{patch}}(\mathbf{x}) + \mathbf{u}_{\text{strain}}, \tag{3.4}$$

with the velocity due to the strain field being $\mathbf{u}_{\text{strain}} = (-2\mu y, -2\mu x)$, where $\mu = \gamma/\omega$ is a non-dimensional measure of the straining field.

The straining field is symmetric and remains unchanged by rotations of π and reflection across $y = x$. If a vortex solution for $\mu > 0$ is reflected across the line $y = x$, the straining field remains the same but the vortex now has the opposite sign of vorticity ($\mu < 0$). These solutions can also be found using our continuation method by decreasing μ through 0 to negative values. This leads to solutions with the semi-major axis aligned with the y-axis. As a result, we consider only $\mu \geqslant 0$.

3.3. *Results*

We performed numerical continuation on the vortex patch with both 128 and 512 points. Using 128 points has the advantage of increased speed, but leads to difficulties converging to solutions with sharp features. Increasing the number of points slows down computation time, but leads to better convergence and solutions further along solution branches. We begin with an overview of the elliptical solutions, then use a perturbation method to switch branches and plot the overall families of solutions for the patch vortex. We then discuss in more detail the first four bifurcating families.

The calculated Moore-Saffman elliptical patch vortex solutions match the analytically known solutions, as shown in Fig. 1. We start with a nearly circular ellipse at the top of the plot, and then use pseudo-arclength continuation to follow the family as the vortices become more elongated. This confirms the expected locations of the bifurcation and fold points. To switch branches onto the bifurcating families, we use the perturbation method discussed in the Appendix. These perturbed solutions are then used as the starting solutions for continuation along the bifurcating families. The bifurcation and fold points predicted by (3.2) are indicated by stars in Fig. 1. We calculated at least part of the bifurcated families at the first eleven different bifurcation points. As the bifurcations occur on more elongated ellipses, we need more points and modes to calculate the bifurcated shapes. It also becomes more difficult to perturb the solutions, because the more elongated shapes of both the elliptical family and the bifurcating branches are very similar. Figure 1 shows the solutions obtained with 512 points and 128 modes (see the Appendix). Solution families end when convergence failed, or solutions were nonphysical (when the vortex boundary crossed itself or when high-frequency oscillations at the Nyquist mode became apparent). The conditions under which a branch of solutions of vortex patches for a similar problem may be continued with respect to a parameter were addressed with mathematical rigour in Gallizio *et al.* (2010).

3.3.1. *Bifurcation for $m = 3$*

The first bifurcation point occurs for $m = 3$ in (3.2). As found by Kamm (1987), this family is not symmetric about the y-axis, and has a teardrop shape. Figure 2 shows an

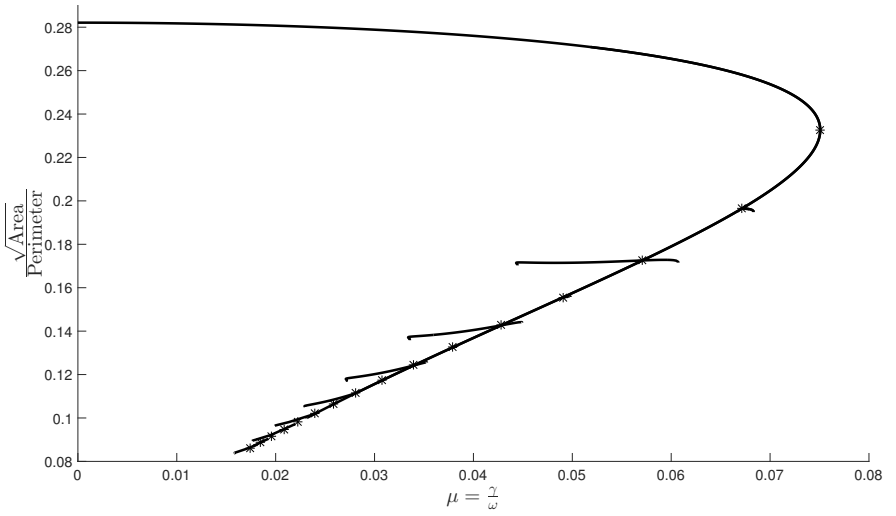

FIGURE 1. Vortex patches in strain, characterized by the relation between μ and the nondimensional shape parameter. The curve spanning the whole range of the latter corresponds to the Moore–Saffman ellipses, the stars show the theoretical bifurcations and fold points, and other curves show families of bifurcated solutions.

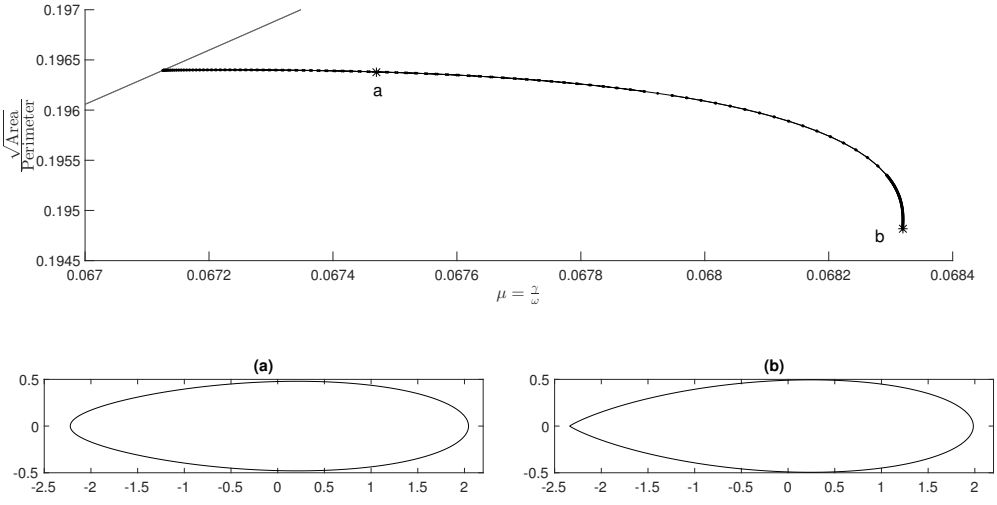

FIGURE 2. Detail of the $m = 3$ bifurcation. The lighter curve shows the elliptical solutions, while the black line and dots show solutions on the bifurcating branch. The left ($\mu = 0.06747$) and right ($\mu = 0.06832$) stars indicate the shapes plotted in (a) and (b), respectively. This family occurs only on the side of the elliptical solutions on which μ is larger.

overview of this family, including an intermediate shape and the limiting shape. Since the code uses splines to rediscretize the points in inverse velocity (see the Appendix), there is always a slightly rounded cusp on small enough scales. It is clear, however, that a limiting cusp shape exists. Cusps on vortex patches were studied previously by Saffman & Tanveer (1982) and Overman (1986).

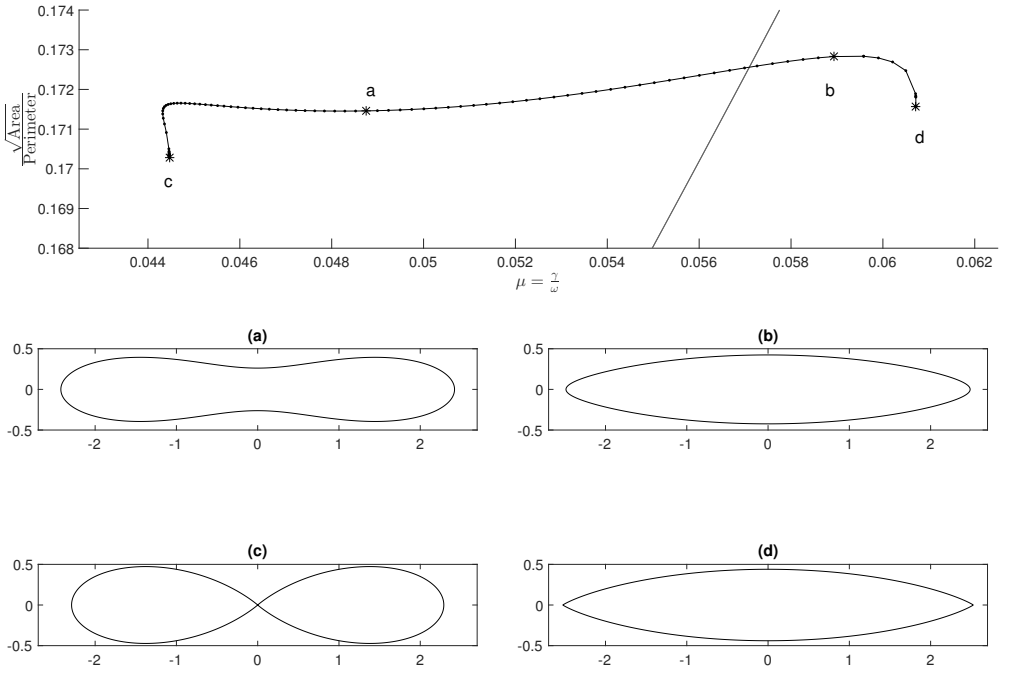

FIGURE 3. Detail of the $m = 4$ bifurcation. The lighter curve shows the elliptical solutions, while the black line and dots show solutions on the bifurcating branch. The stars show the limiting solutions which are plotted in a ($\mu = 0.04875$), b ($\mu = 0.05893$), c ($\mu = 0.04446$), and d ($\mu = 0.06072$).

The asymmetry in this shape necessitates some discussion of the symmetries of the background straining field. In Fig. 2, we show shapes that have the cusp on the left and the rounded side on the right. The numerical continuation also calculated shapes that had the cusp on the right and the rounded side on the left, and these shapes are in fact identical up to reflection. Given the symmetry of the strain, there is no preferred direction for these shapes, and one can obtain vortices with cusps either to the left or right.

3.3.2. *Bifurcation for $m = 4$*

The next bifurcation point occurs for $m = 4$ in (3.2). This family has two different branches, depending on whether μ is increasing or decreasing. When μ increases (which can be thought of as a decrease in the strength of the vortex patch, or an increase in the strength of the straining field), the shapes change from an ellipse to a doubly symmetric football shape with two cusps (Fig. 3(a) and (c)). When μ decreases, the shapes start to pinch-off at the centre while remaining doubly symmetric (Fig. 3(b) and (d)). Kamm (1987) was able to calculate the cusped shape for larger values of μ, but was unable to calculate the vortex shapes with the pinch-off.

3.3.3. *Bifurcation for $m = 5$*

Continuing along the elliptical branch, the next bifurcation occurs at $m = 5$. As with the previous odd m value, this branch only occurs on the side of the elliptical family with larger values of μ, and again has symmetry about the x-axis but not the y-axis. As

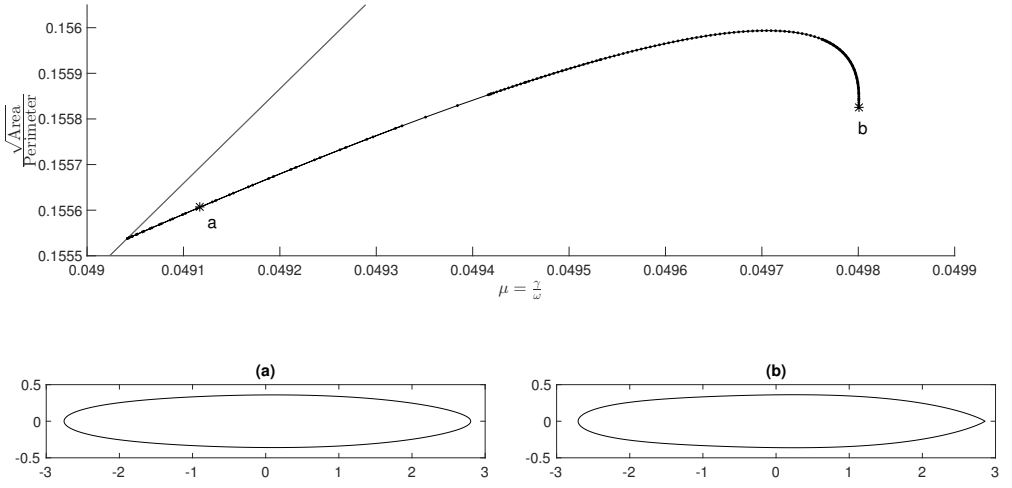

FIGURE 4. Detail of the $m = 5$ bifurcation. The lighter curve shows the elliptical solutions, while the black line and dots show solutions on the bifurcating branch. The left ($\mu = 0.04912$) and right ($\mu = 0.04980$) black stars show the solutions which are plotted in (a) and (b), respectively.

before, one side of the vortex is rounded, and the other side becomes cusped. However, as this shape is more elongated, the maximum width occurs closer to the cusp than the rounded side. This branch, shown in Fig. 4, was the last calculated by Kamm (1987).

3.3.4. *Bifurcation for $m = 6$*

The next even bifurcation occurs for $m = 6$, and it begins to show the pattern for the even bifurcating families. Again, the family with smaller μ has pinch-offs, but this time there are two, whereas for $m = 4$ there was only one. For larger μ, the family again has two cusps, but is more elongated in the middle. These shapes and the family are shown in Fig. 5.

3.3.5. *Later bifurcating families*

The pattern of an increase in the number of pinch-offs and elongation of the cusped shapes continues as m increases. For example, Fig. 6 shows the last shape for the branch with seven pinch-offs, which occurs for $m = 16$. For even values of m, the bifurcating family with smaller μ will have $m/2 - 1$ pinch-offs.

4. Vortex sheet

4.1. *Problem Description*

Vortex sheets are curves or surfaces of discontinuity in flow velocity. While a vortex patch has no singularities in the vorticity, a vortex sheet corresponds to a delta function with argument normal to the contour. According to Saffman (1992), a vortex sheet induces the following velocity for points not on the vortex sheet:

$$u - \mathrm{i}v = \frac{-\mathrm{i}}{2\pi} \int \frac{\kappa(s,t)\,\mathrm{d}s}{z - Z(s,t)}, \tag{4.1}$$

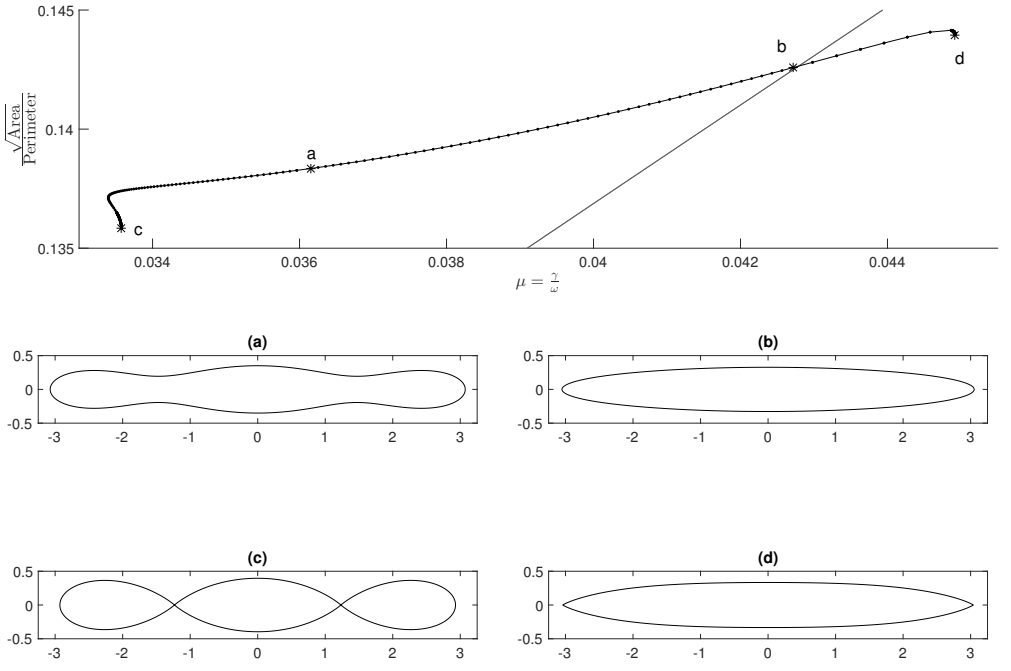

FIGURE 5. Detail of the $m = 6$ bifurcation. The lighter curve shows the elliptical solutions, while the black line and dots show solutions on the bifurcating branch. The stars show the solutions that are plotted in a($\mu = 0.03615$), b ($\mu = 0.04271$), c ($\mu = 0.03358$), and d ($\mu = 0.04492$).

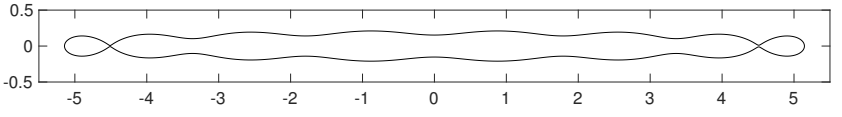

FIGURE 6. Vortex shape for the bifurcating family with smaller μ at $m = 16$, showing 7 developing pinch-offs.

where $(u(x, y), v(x, y))$ is the induced velocity, $z = x + \mathrm{i}y$ is the point of interest, Z is position along the sheet, and κ and Z are parameterized by arclength and time. The quantity κ is the difference in speed across the vortex sheet. This integral is the same as the flow field due to a set of point vortices along the contour with appropriate circulation. For points on the vortex sheet, that integral becomes a principal value integral, and the induced velocity gives the velocity of the vortex sheet. To obtain the limiting velocity when approaching the sheet from the right or left, half the velocity jump is added or subtracted to the principal value:

$$u - \mathrm{i}v = \frac{-\mathrm{i}}{2\pi} \int \frac{\kappa(s,t)\,\mathrm{d}s}{z - Z(s,t)} \pm \frac{\kappa}{2}\,(x' - \mathrm{i}y')\,, \tag{4.2}$$

where x' and y' are the components of the unit tangent vector of the boundary, and s is arclength. The $\pm$ signs refer to the right and left sides of the curve as it is traversed in the positive sense.

Previous research has focused on the hollow vortex, which is a vortex sheet surrounding a constant pressure region. This corresponds to no flow inside the vortex (as can be seen by the maximum principle), and is equivalent to setting $\rho_{in} = 0$ inside the vortex in (2.9). The hollow vortex in a straining field was obtained by Llewellyn Smith & Crowdy (2012) using a conformal mapping from the unit disc to the fluid outside the vortex. The closed form of the conformal map from the physical z-plane to the mapping ζ-plane that gives the shape of the vortex is

$$z(\zeta) = a\left[\frac{1}{\zeta} - 2\mathrm{i}\beta\zeta + \frac{\beta^2}{3}\zeta^3\right], \tag{4.3}$$

where a is a length scale. The boundary of the vortex is at $|\zeta| = 1$, and

$$\beta = -\frac{\mu_h}{1+\sqrt{1-\mu_h^2}}, \qquad \mu_h = \frac{8\pi\gamma a^2}{\Gamma}, \tag{4.4}$$

where γ is the strength of the straining field and Γ is the circulation of the vortex sheet. From the conformal mapping, it is clear that as we go around the unit circle in an anticlockwise direction, we traverse the vortex boundary in a clockwise direction. Note that this formulation corresponds to a straining field with principal axes oriented along $y = \pm x$. We will use the Moore–Saffman choice of principal axes along the coordinate axes in what follows.

4.2. *Results*

Figure 7 shows the agreement between the calculation and the analytical solutions from Llewellyn Smith & Crowdy (2012). The inset shows the calculated vortex shapes with 256 points at $\lambda_s = 0.01706, 0.08923, 0.12431, 0.09136$ and the analytical limiting shape at pinch-off. The parameter $\lambda_s = \gamma L/q$ is a non-dimensional measure of the straining field γ compared to the velocity on the boundary q, with L a reference length. It is related to μ_h in (4.4). The analytical shapes have been rotated to align with the straining field, and plotted along with the black calculated shapes; and the two are indistinguishable. Convergence becomes difficult as the distance between points becomes similar to the width of the shape, so the method was not able to converge at the pinch-off shape.

5. Sadovskii vortex

5.1. *Governing parameters*

Our solution method takes the velocity field of the steady solution to be the superposition of the velocity due to the vortex patch, vortex sheet and the straining field. To compare sheet and patch solutions, as well as all Sadovskii solutions in between, requires two non-dimensional parameters. To calculate the circulation outside the vortex, we use the definition

$$\Gamma_{out} = \oint_{\partial S} \mathbf{u}_{out} \cdot \mathrm{d}\mathbf{s}, \tag{5.1}$$

where $\mathbf{u}_{out}$ is the total velocity just outside the vortex boundary and ∂S is the boundary of the vortex. Since the flow is irrotational outside the vortex, any contour that encloses the vortex will give the same value for Γ_{out}. To calculate Γ_{in}, we again use the definition of circulation, but evaluate the contour just inside the vortex sheet on the boundary:

$$\Gamma_{in} = \oint_{\partial S} \mathbf{u}_{in} \cdot \mathrm{d}\mathbf{s}. \tag{5.2}$$

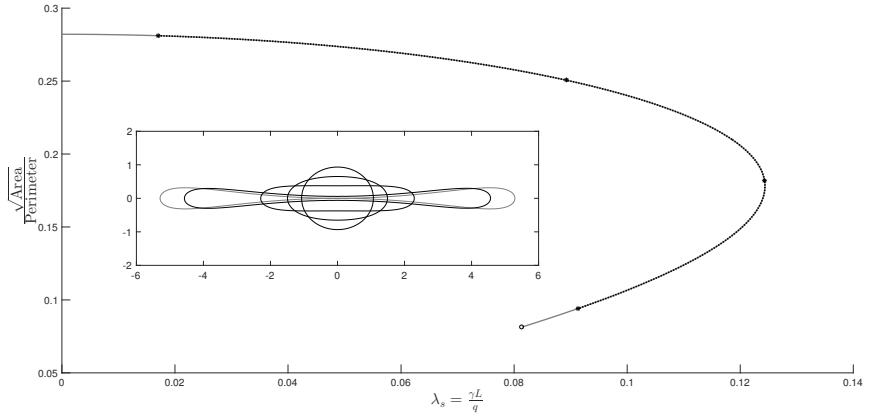

FIGURE 7. Hollow vortex shapes: the shape parameter is plotted against λ_s, a nondimensional parameter relating the straining field strength to the vortex sheet strength. The solid line shows the results obtained from Llewellyn Smith & Crowdy (2012), while the dotted line shows the numerical solution. The inset shows calculated vortex shapes plotted at the points indicated by stars. The circle indicates the limiting analytical vortex shape, plotted in the inset in grey.

An equivalent way to write these circulations to show the effect of the different parts of the vortex is

$$\Gamma_{in} = \omega A, \qquad \Gamma_{out} = \Gamma_{in} + \oint_{\partial S} \kappa \, \mathrm{d}s, \tag{5.3}$$

where A is the area of the vortex patch and κ is the vortex sheet strength.

For the parameter relating the vortex patch strength to the vortex sheet strength, we use the parameter

$$\Lambda = \frac{\Gamma_{in}}{\Gamma_{out}}. \tag{5.4}$$

The vortex patch has $\Lambda = 1$, the vortex sheet has $\Lambda = 0$, and Sadovskii vortices lie in the range $0 < \Lambda < 1$. For the parameter relating the straining field strength to the vortex strength, we use

$$S_r = \frac{\gamma L^2}{\Gamma_{out}}. \tag{5.5}$$

This parameter goes to 0 for solutions that are circular, where the vortex is much stronger than the straining field, and it has an upper bound for all patch, sheet, and Sadovskii solutions. This parameter is similar to the parameter μ_h used in Llewellyn Smith & Crowdy (2012); see (4.4). These two parameters, Λ and S_r, allow us to plot all Sadovskii solutions in a finite area in the parameter space.

5.2. *Results*

Figure 8 shows the manifold of Sadovskii vortices. While the manifold is a three-dimensional surface, the figure shows only points corresponding to specific solutions that we calculated. Each point shown on the manifold corresponds to a vortex shape. At $\Lambda = 1$, it includes the vortex patch data, and at $\Lambda = 0$, it includes the vortex sheet data. The crosses mark calculated bifurcation points, while the stars are the expected bifurcation points of the patch family from Moore & Saffman (1971). It is hard to absorb all the details of the Sadovskii solutions from Fig. 8, so the rest of this section discusses the interesting parts of the solution manifold.

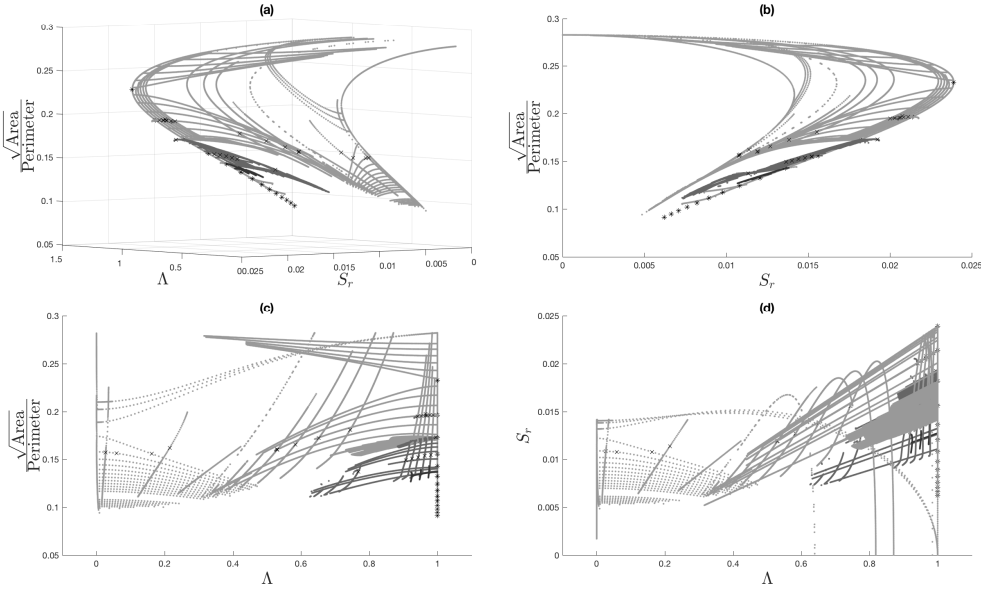

FIGURE 8. Overview of the Sadovskii solution manifold. Each panel shows a different view. Different shades of grey are associated with different families of solutions; these families connect to each other for $\Lambda = 1$, but are separate for $\Lambda < 1$. Solutions near $\Lambda = 1$ were calculated using the patch nondimensionalization, while solutions near $\Lambda = 0$ were calculated using the sheet nondimensionalization (see the Appendix).

The bifurcation point for the patch case for $m = 4$ was seen to lead to a split in the solution families of the Sadovskii vortex. While the variables Λ and S_r are convenient for showing the entire manifold, the details of the behaviour as one moves away from the vortex patch solutions are more easily discussed in terms of $\lambda = q/\omega L$ and $\mu = \gamma/\omega$. As soon as $\lambda > 0$ (i.e. $\Lambda < 1$), the solution curves are no longer all connected. Instead, as shown in Fig. 8 for the $m = 4$ bifurcation, the elliptical solutions with larger shape parameter remain joined to the bifurcated solutions with smaller μ, which are the pinch-off solutions, while the elliptical solutions with smaller shape parameter remain joined to the solutions with larger μ. The latter tend to cusped football solutions in the patch case, but as will be shown later, for $\lambda > 0$, while the solutions have the same overall shape, they do not develop cusps. The pinch-off solutions connect to the vortex sheet solutions when $\Lambda = 0$, while the football solutions cannot, since it is the pinch-off solutions that become the vortex sheet solutions found by Llewellyn Smith & Crowdy (2012). The football solutions presumably cease to exist at a finite positive value of Λ, but we did not attempt to find the final solutions.

Figure 9 shows the split between the families occurring. As λ increases, the families get farther apart. In (a), the vortex patch case, the families are still connected. In (b) with $\lambda = 0.05059$, with the dashed line showing the more elongated family; (c) and (d) correspond to $\lambda = 0.07190$ and $\lambda = 0.08880$ respectively.

This split in the solution families at even m bifurcation points is important. It explains the difference between the vortex patch and vortex sheet bifurcation diagrams. In the case of the vortex patch, there exist bifurcation points with even m values, and at these points the elliptical solution family is crossed by two branches, one of which has a pinch-off point and the other which has cusps at both ends. The addition of any amount of vortex sheet ($\Lambda < 1$) removes the cusps, and in doing so also separates these families. What had

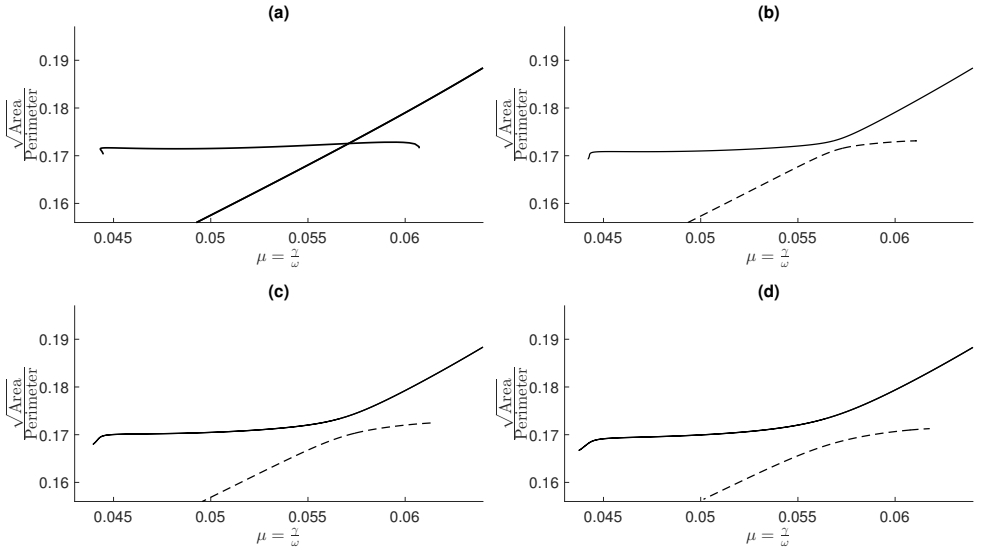

FIGURE 9. Split in Sadovskii vortex families near the $m = 4$ bifurcation point. Patch solutions with $\lambda = 0$ are shown in (a). In (b), (c), and (d), Sadovskii solutions are shown at constant values of λ. In (b), (c), and (d), the upper family is shown in the solid line and the more elongated family is shown by the dashed line. As λ increases, these families get further from each other.

previously been a single elliptical family is split into two, with the more circular shapes staying connected to the shapes that include a pinch-offs. The more elongated elliptical shapes stay connected to the family with cusps at both ends. This pattern continues at each even value of m on the patch family. It seems that the only solutions that exist for $\Lambda = 0$ are the upper branch, which connects the circular solutions to the solutions with a single pinch-off.

5.3. *Connecting branch*

The connecting branch is shown in Fig. 10. This is the portion of the Sadovskii solution manifold that connects the vortex patch solutions with the vortex sheet solutions. As the figure shows, this only includes the solutions that were circular or had a single pinch-off, but does not include those that had cusps at both ends, were more elongated, or had more than one pinch-off.

Generally, it seems the vortex sheet leads to more rounded shapes, as the vortex sheet cannot exist at cusps (Tanveer, private communication; see also Saffman & Tanveer 1982). As Λ is decreased from 1, the sharp features that exist on the limiting patch vortex shapes become smooth. In the case of the circular vortices, which have a large shape parameter but small S_r, the shapes do not change. This is because they have circular vortices for the limiting cases of the patch and sheet vortices, and all Sadovskii vortices in between. This the expected result, since a circular shape is a known solution for a vortex with no other flow field.

The effect of the combination of the two sources of circulation is evident in the limiting shapes of vortices with a single pinch-off. This type of vortex exists for both the patch and sheet cases, although with different shapes. In Fig. 11, the last converged shapes are shown for various values of Λ. In the patch case, the limiting shape had sharp cusps at the pinch-off points, shown in (a). In the vortex sheet case, there is a much smoother transition from the ends to the pinch-off in the center, shown in (d). Beginning at the

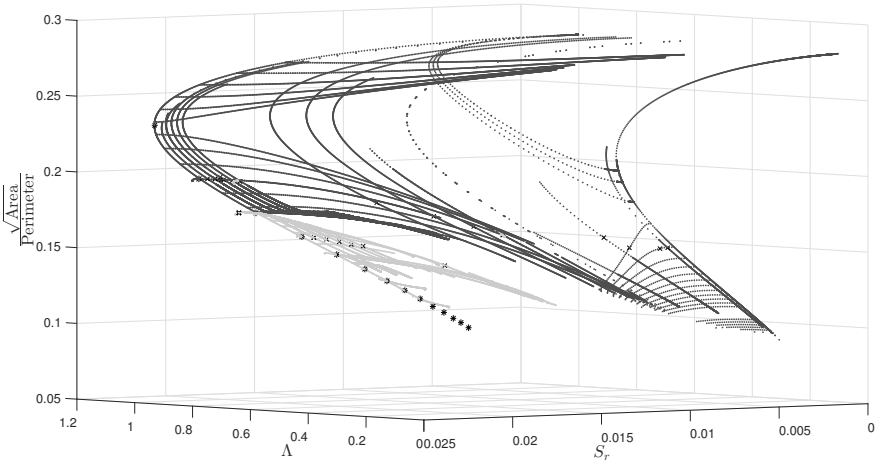

FIGURE 10. The connection between the connecting portion of the patch vortex solutions and the entire vortex sheet solution family. The connecting branch is plotted in the darker colour, while the rest of the Sadovskii solutions are plotted in light grey.

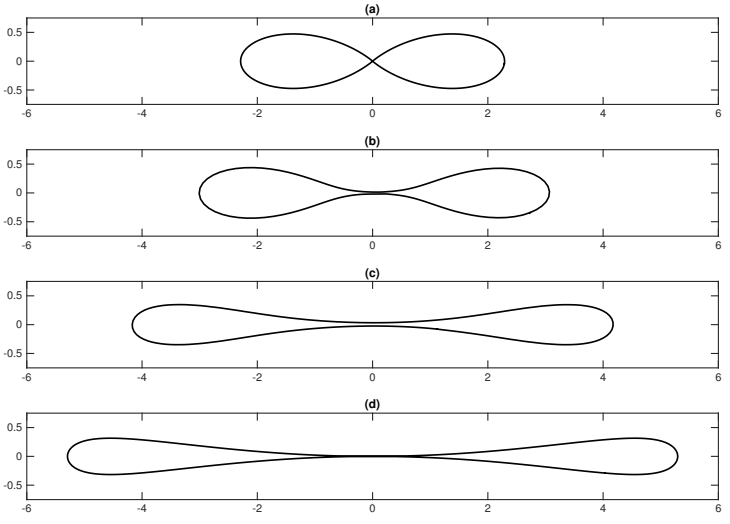

FIGURE 11. A plot of the closest shapes to pinch-off for various sheet and vorticity strengths. In (a), the vortex patch shape, with $\Lambda = 1$, using 512 points (see Fig. 3(c)). In (b), the last converged Sadovskii shape with $\Lambda = 0.62533$, using 128 points. In (c), the last converged Sadovskii shape with $\Lambda = 0.29238$, using 256 points. In (d), the theoretical limit for the vortex sheet, from Llewellyn Smith & Crowdy (2012) (see Fig. 7).

vortex patch, as the vortex sheet strength is increased, the shape of the vortex in the area of the pinch-off smooths out and begins to look more like the vortex sheet shape, as shown in (b) and (c). The Sadovskii shapes did not converge all the way to the pinch-off point. The code had difficulty converging when the distance between the boundary points became similar to the minimum width of the shape.

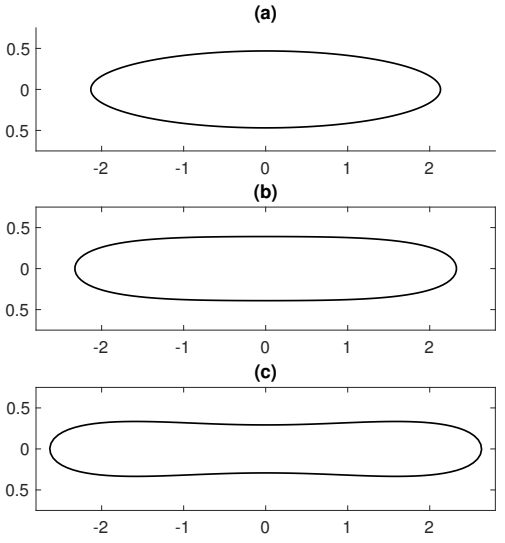

FIGURE 12. The shapes of Sadovskii vortices at the $m = 3$ bifurcation point at three different locations on the solution manifold. In (a), the vortex at the bifurcation point is shown for $\Lambda = 0.98807$ and $S_r = 0.02110$. In (b) is the vortex at $\Lambda = 0.74368$, $S_r = 0.01555$. In (c), the vortex at $\Lambda = 0.53038$, $S_r = 0.01192$.

5.3.1. *Bifurcation for $m = 3$*

While the bifurcation point for $m = 4$ caused a split in the solution families for $\Lambda < 1$, the asymmetric bifurcating family for $m = 3$ remained attached to the connecting family. This pattern of splitting of families at even numbered values of m, while the bifurcating families at odd values of m remain attached to the family, seems to continue for higher values of m on other branches.

Figure 12 shows the vortex shapes at the $m = 3$ bifurcation point for three different points on the solution manifold. As the bifurcation points move to smaller values of the shape parameter and strain ratio, they take on more of the characteristics of the shapes that were originally on the bifurcating branch for $m = 4$ (see Fig. 3(a)), showing the flattening out and then beginnings of the pinch-off in the center.

To calculate the shapes of the asymmetric vortices on the bifurcating families for $m = 3$, we calculated a perturbed solution near the bifurcation point, then used this perturbed solution as a starting point for continuation in μ. Using increased weights on the centroid and area constraints ($a = b = c = 10^5$ instead of 100) gave better convergence to solutions.

In the vortex patch case, the limiting shape for this solution branch had a cusp, shown in Fig. 13(a). As the vortex sheet strength increases, the vortex can no longer support a cusp. Instead, the effect of the sheet is to round the cusp out, and it begins to extend in a thin finger. As the straining field and vortex sheet become stronger (but remains in the large Λ regime), this thin finger also begins to curve. This shape is shown in Fig. 13(b).

As Λ decreases (and the sheet strength increases), the vortex shape becomes more rounded, with a wider minimum width. Figure 14(a) shows the symmetric solution at the bifurcation point when nearly half the circulation is due to the vortex sheet. Figure 14(b) shows the last converged asymmetric solution on the bifurcating branch, showing the wider radius of curvature where the cusp or finger existed in vortices with weaker vortex sheets (Figure 13). We calculated the asymmetric solutions for many solution

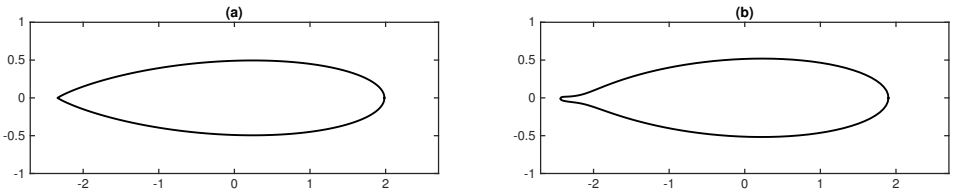

FIGURE 13. Comparison of patch and Sadovskii asymmetric shapes. In (a), the limiting shape for the patch vortex ($\Lambda = 1$) showing the cusp. This comes from the bifurcating family for $m = 3$. In (b), the last converging shape for the related bifurcating family at ($\Lambda = 0.93196$, $S_r = 0.02051$). The vortex sheet forces a round shape, and in this case begins to extend the side where the cusp was. There is also a slight curve to the narrow finger that occurs where the cusp was. This curve becomes more pronounced with increasing S_r.

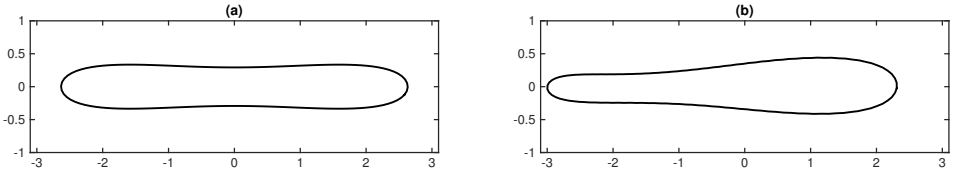

FIGURE 14. Asymmetric branch for a Sadovskii vortex. In (a), the symmetric shape at the bifurcation point ($\Lambda = 0.53038$, $S_R = 0.01192$). In (b), the last converged shape for the Sadovskii vortex ($\Lambda = 0.52351$, $S_r = 0.01191$) showing the asymmetry. This comes from the bifurcating family for $m = 3$.

families that had the bifurcation point, but did not attempt to discover where these asymmetric families ceased to exist as Λ tends to zero.

5.4. *Branches for $m = 4$ and $m = 6$*

The natures of the $m = 4$ and $m = 6$ bifurcation points are the same: the top family of more circular vortices remains attached to the family with pinch-offs, while the family of patch vortices with sharp cusps becomes attached to the lower family of more elongated shapes. Now the lower family (dashed line) in Fig. 9 is attached to the family with two pinch-off points (see Fig. 15). However, neither of these families exists all the way to $\Lambda = 0$. The separation is shown in Figure 15, while the family between $m = 4$ and $m = 6$ are shown in Figure 16.

The behaviour of the cusps is similar to the single cusp in the $m = 3$ branch. In this case, it occurs on both sides, and it doesn't appear to exhibit the slight curve shown in Fig. 13(b). As the sheet strength is increased, thin fingers again extend outward from where the cusps were. As the sheet continues to increase in strength, these fingers get wider at the edges, and the shape appears closely related to one with two pinch-off points (see Fig. 18). As the sheet strength increases, there is less variance in vortex shape between the edges of the family. In Fig. 17, we show the cusped patch shape and compare it to a Sadovskii shape showing the bulging fingers on both ends.

As Fig. 18 shows, as the vortex sheet strength increases, the pinch-off points on the $m = 6$ branch are smoothed out much as occurs in the hollow case. No solutions for

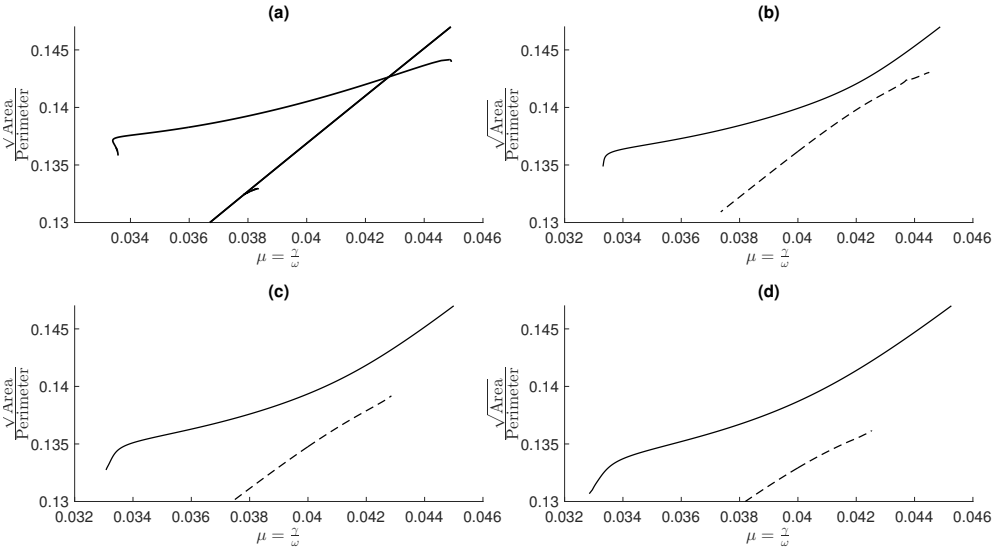

FIGURE 15. Split in Sadovskii vortex families near the $m = 6$ bifurcation point. Patch solutions with $\lambda = 0$ are shown in (a). In (b), (c), and (d), Sadovskii solutions are shown at constant values of $\lambda = 0.05051$, 0.07191, 0.08880, respectively. In (b), (c), and (d), the family between $m = 4$ and $m = 6$ is shown in the solid line and the more elongated family is shown by the dashed line. As λ increases, these families get farther from each other.

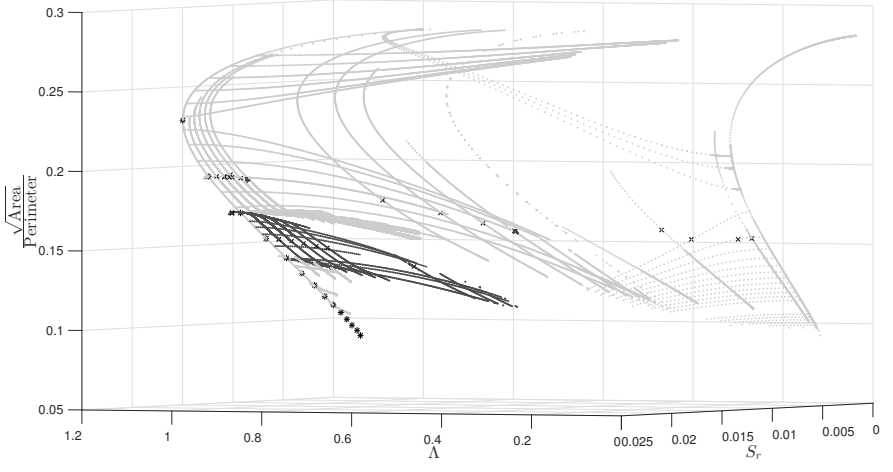

FIGURE 16. The family of Sadovskii solutions connecting the doubly cusped solutions at the $m = 4$ patch bifurcation with the solutions with two pinch-off points at the $m = 6$ patch bifurcation is shown in the darker color. All other Sadovskii solutions are shown in lighter grey.

$\Lambda < 0.6$ converged for this family between $m = 4$ and $m = 6$. It is likely that this family ends at a point where the only solution is at the $m = 5$ bifurcation point.

As Λ is decreased, the shape of the vortices at the bifurcation point began to show the signature of two pinch-off locations, as shown in Fig. 19. The two shapes, one with the two sharp ends, and one with the two pinch-off points, become more similar as the vortex sheet becomes stronger, as can be seen from the shape of Fig. 19(b).

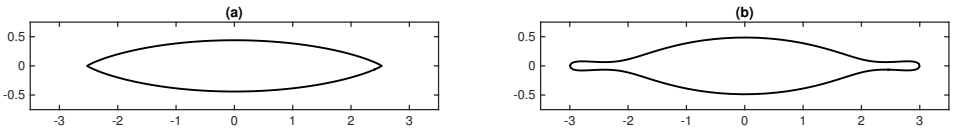

FIGURE 17. Comparison of patch and Sadovskii shapes for $m = 4$ branch. In (a), the limiting shape for the patch vortex ($\Lambda = 1$, $\mu = 0.06072$) showing the cusps (see Fig. 3(d)). In (b), the last converging shape for the related bifurcating family at ($\Lambda = 0.75920$, $S_r = 0.01326$). The vortex sheet forces a round shape, which leads to the skinny fingers on each side where the cusps had been. This shape is the end of the family of solutions represented by the dashed lines in Fig. 9.

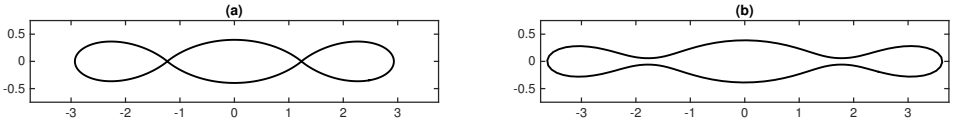

FIGURE 18. Comparison of patch and Sadovskii shapes for $m = 6$ branch. In (a), the limiting shape for the patch vortex ($\Lambda = 1$, $\mu = 0.03358$) showing the sharp pinch points (see Fig. 5(c)). In (b), the last converging shape for the related bifurcating family at ($\Lambda = 0.71162$, $S_r = 0.00775$). The vortex sheet leads to pinch-off points that are closer to those of the hollow vortex, or the vortex sheet alone.

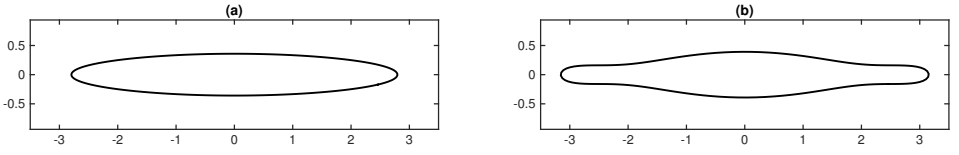

FIGURE 19. Sadovskii vortex shapes for $m = 5$ bifurcation points. In (a), the shape at $\Lambda = 0.98070$, $S_r = 0.015224$. In (b), the shape at $\Lambda = 0.76783$, $S_r = 0.01134$.

Figure 20 shows the asymmetric shape of a vortex on the bifurcating family, at $\Lambda = 0.76452$, $S_r = 0.01190$. One side looks like the symmetric shape in Fig. 19(b), while the other side looks more like the shape in Fig. 17(b).

6. Conclusions

We have obtained the shapes of steady Sadovskii vortices in strain. Using numerical continuation, we were able to trace out the solution manifold described by two parameters, taken here to be $\Lambda = \Gamma_{in}/\Gamma_{out}$ and $S_r = \gamma L^2/\Gamma_{out}$. The limiting cases of the vortex patch and vortex sheet are recovered and match previously obtained solutions.

For vortex patches, we obtained families that bifurcate from the elliptical solutions, as

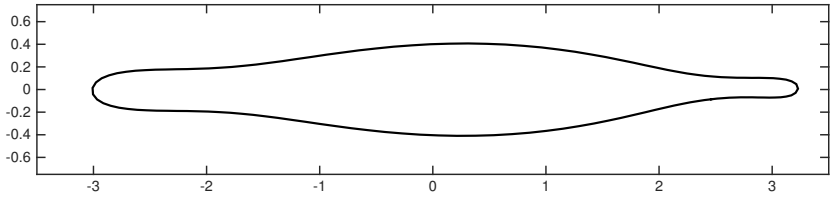

FIGURE 20. Sadovskii vortex asymmetric shape at the $m = 5$ bifurcation point, with $\Lambda = 0.76452$, $S_r = 0.01190$. One side of this asymmetric vortex looks like the shape on the symmetric family, while the other side is narrower. Compare this to the patch shape in Fig. 4(b).

in Kamm (1987). We took the calculations further than before, and found that families at higher values of m had more pinch-offs. Even bifurcation points led to asymmetric vortex shapes that extended only into larger values of S_r. Odd bifurcation points lead to families that extend in both directions along S_r, with either a pinch-off point or a sharp cusp at either end.

For Sadovskii vortices, we calculated points on the solution manifold in the parameter space. The addition of the vortex sheet to the vortex patch solutions immediately leads to a split in the solution manifold at bifurcation points for even values of m. It is this splitting of the families that leads to the much simpler solution branch for the vortex sheet. The more circular vortex patch solutions remain connected to the family with a single pinch-off at $m = 4$, while becoming disconnected from the more elongated elliptical solutions and the family with cusps at both ends.

The addition of the vortex sheet to the vortex patch smooths out sharp features. As the vortex sheet strength is increased, the radius of curvature also increases, so features such as fingers become wider and less pronounced. This leads to a shrinking of the solution manifold, as the more deformed shapes do not seem to exist for strong enough vortex sheet strengths and the existing shapes become more similar. It also appears that the more elongated families that exist below the $m = 4$ family only exist for small values of the vortex sheet strength, which explains why they do not appear as vortex sheet solutions.

We have shown that our approach successfully calculates the known vortex patch and sheet shapes and used it to find new shapes. It can also be applied to cases with rotational background flows by decomposing the flow appropriately. For example it can be used to obtain the hollow vortex in shear solutions of Zannetti *et al.* (2016). Other possible situations include multiple vortex equilibria to desingularize the classical rotating same-sign point vortices.

Future work may investigate the stability of the steady solutions we have calculated. This will be particularly interesting in the presence of surface tension, which may serve to mitigate the possibility of Kelvin-Helmholtz instability in the stagnant case when the inner fluid has non-zero density.

This work was partially supported by NSF award CMMI-0970113. A UCSD Collaboratory award also provided support. Helpful discussions with Darren Crowdy, Saleh Tanveer and Paolo Luzzatto-Fegiz are acknowledged.

Appendix A. Numerical method

Numerical continuation is performed using a predictor-corrector scheme for pseudo-arclength continuation. For details on such schemes, see Govaerts (2000). Since we use an inverse velocity formulation, points are clustered in areas where the speed on the vortex sheet is lower. The inverse velocity discretization (see Luzzatto-Fegiz & Williamson (2011)) is

$$\tilde{s}(s) = A \int_0^s \frac{\mathrm{d}s'}{|\mathbf{u}(s')|}, \tag{A 1}$$

where A is chosen so $0 \leqslant \tilde{s} \leqslant 2\pi$, s is the arclength, and $\mathbf{u}$ is the velocity in the reference frame of interest. This method assumes that the solution is a superposition of three velocity fields: the background straining flow, the vortex patch, and the vortex sheet. Given a vortex solution, the basic method for the continuation is:

(i) Rediscretize points by inverse velocity using cubic splines;
(ii) Predict new vortex solution using null-space of Jacobian;
(iii) Correct the guess using Gauss–Newton Solver to converge to actual solution;
(iv) Repeat until convergence is achieved.

To reduce the number of variables in the problem, the boundary points of the vortex are only allowed to move along the normal vectors. We are calculating the scalar functions α and α_k, where

$$x_i^n = x_i + \alpha(\tilde{s}_i) n_x, \tag{A 2}$$
$$y_i^n = y_i + \alpha(\tilde{s}_i) n_y, \tag{A 3}$$
$$\kappa_i^n = \kappa_i + \alpha_\kappa(\tilde{s}_i). \tag{A 4}$$

The (x_i, y_i) are the boundary points and κ_i represent the vortex sheet strengths at the point. The functions α and α_κ are calculated based on their Fourier coefficients, where

$$\alpha(\tilde{s}_i) = \frac{1}{N} \sum_{j=-N/2}^{N/2-1} \hat{\alpha}_j \mathrm{e}^{2\pi \tilde{s}_i j \mathrm{i}/N}, \tag{A 5}$$

with $\hat{\alpha}_j$ the complex Fourier coefficients. While we define the shapes using N points, we only allow M modes in the adjustment functions α and α_κ, where $M \leqslant N$, so we require that $\hat{\alpha}_j = 0$ for $|j| > M$. We are using M as a way to set the maximum wavenumber we keep when we apply an ideal low-pass filter to the adjustment of the shape. A similar approach is used for α_κ. The unknowns that are actually found by the predictor-corrector method are the Fourier coefficients $\hat{\alpha}$ and $\hat{\alpha}_\kappa$.

The two boundary conditions used to calculate these Fourier coefficients are the Fourier transforms of the kinematic condition (2.6) and the dynamic (Bernoulli) condition (2.9). The total velocity is $\mathbf{u} = \mathbf{u}_{\text{patch}} + \mathbf{u}_{\text{sheet}} + \mathbf{u}_{\text{strain}}$, where $\mathbf{u}_{\text{patch}}$ is calculated from (3.3) and $\mathbf{u}_{\text{sheet}}$ is calculated from (4.2). The integrals in these calculations are calculated using the trapezoidal rule, applied at the midpoints to avoid poles at the points of interest. The values at midpoints are calculated using Fourier transforms, as in Baker & Nachbin (1998). Just as the average velocity on the vortex boundary is used for the discretization of the points, the same average velocity, which is the principal value integral in (4.2), is used in the kinematic condition. This works because the additional term that comes from the vortex sheet cannot affect the normal velocity.

Depending on the solution regime, different nondimensionalizations of these boundary conditions were used. For solutions near the vortex patch, the equations were nondimen-

sionalized using

$$x = Lx^*, \quad u = L\omega u^*, \quad \mu = \frac{\gamma}{\omega}, \quad \lambda = \frac{q}{\omega L}, \quad \rho = \frac{\rho_i}{\rho_o}, \tag{A 6}$$

while solutions near the vortex sheet were nondimensionalized using

$$x = Lx^*, \quad u = L\gamma u^*, \quad \mu_s = \frac{\omega}{\gamma}, \quad \lambda_s = \frac{\gamma L}{q}, \quad \rho = \frac{\rho_i}{\rho_o}. \tag{A 7}$$

These nondimensionalizations are used for numerical purposes and are not needed in the discussion of § 5.

We actually solve a constrained problem, in which each of the boundary conditions has added terms to ensure the vortex is centered at the origin and has a fixed area. The area and centroids are calculated using the trapezoidal rule from

$$A = \oint x \frac{\mathrm{d}y}{\mathrm{d}\tilde{s}}\,\mathrm{d}\tilde{s}, \qquad x_C = -\frac{1}{2A}\oint x^2 \frac{\mathrm{d}y}{\mathrm{d}\tilde{s}}\,\mathrm{d}\tilde{s}, \qquad y_C = \frac{1}{2A}\oint y^2 \frac{\mathrm{d}x}{\mathrm{d}\tilde{s}}\,\mathrm{d}\tilde{s}. \tag{A 8}$$

The constraints added to (2.6) and (2.9) are

$$ax_c t_1(s_r) + by_c t_2(s_r) + c(A - \pi)t_3(s_r) = 0, \tag{A 9}$$

where a, b and c are weights and t_1, t_2, and t_3 are the first three Legendre polynomials evaluated at $s_r = (\tilde{s}/\pi) - 1$. We used weights of $a = b = c = 100$, unless otherwise noted, to ensure that the area and centroid conditions were satisfied. These constraints are added before the Fourier transform is taken.

Results were checked to make sure the area and centroid constraints were satisfied. After reviewing the results, we found that high-frequency Nyquist mode oscillations or nonphysical (self-intersecting) shapes occurred when $|x_c| > 5 \times 10^{-7}$, $|y_c| > 5 \times 10^{-7}$, or $|A - \pi| > 5 \times 10^{-6}$. Only solutions with centroid and area errors smaller than these values were retained.

Branch switching was performed by solving a perturbed problem, where a constant term was added to the boundary conditions. This perturbation causes a splitting of the families at the bifurcation point, allowing continuation to go smoothly from one branch to the other. Once on the other branch, the perturbation was removed and the actual problem was solved, using as a starting guess the perturbed solution on the new branch.

REFERENCES

Ardalan, K., Meiron, D. I. & Pullin, D. I. 1995 Steady compressible vortex flows: the hollow-core vortex array. *J. Fluid Mech.* **301**, 1–17.

Baker, G. & Nachbin, A. 1998 Stable methods for vortex sheet motion in the presence of surface tension. *SIAM J. Sci. Comp.* **19**, 1737–1766.

Baker, G. R., Saffman, P. G. & Sheffield, J. S. 1976 Structure of a linear array of hollow vortices of finite cross-section. *J. Fluid Mech.* **74**, 469–476.

Batchelor, G. K. 1956*a* On steady laminar flow with closed streamlines at large Reynolds number. *J. Fluid Mech.* **1**, 177–190.

Batchelor, G. K. 1956*b* A proposal concerning laminar wakes behind bluff bodies at large Reynolds number. *J. Fluid Mech.* **1**, 388–398.

Bunyakin, A. V., Chernyshenko, S. I. & Stepanov, G. Yu. 1996 Inviscid Batchelor-model flow past an airfoil with a vortex trapped in a cavity. *J. Fluid Mech.* **323**, 367–376.

Bunyakin, A. V., Chernyshenko, S. I. & Stepanov, G. Yu. 1998 High-Reynolds-number Batchelor-model asymptotics of a flow past an aerofoil with a vortex trapped in a cavity. *J. Fluid Mech.* **358**, 283–297.

Chernyshenko, S. I. 1998 Asymptotic theory of global separation. *Appl. Mech. Rev.* **51**, 523–536.

Chernyshenko, S. I., Galletti, B., Iollo, A. & Zannetti, L. 2003 Trapped vortices and a favourable pressure gradient. *J. Fluid Mech.* **482**, 235–255.

Crowdy, D. G. & Green, C. C. 2011 Analytical solutions for von Kármán streets of hollow vortices. *Phys. Fluids* **23**, 126602.

Deem, G. S. & Zabusky, N. J. 1978 Vortex waves: stationary "V states", interactions, recurrence and breaking. *Phys. Rev. Lett.* **40**, 859–862.

Gallizio, F., Iollo, A., Protas, B. & Zannetti, L. 2010 On continuation of inviscid vortex patches. *Physica D* **239**, 190–201.

Govaerts, W. 2000 *Numerical Methods for Bifurcations of Dynamical Equilibria*. Philadelphia, PA: Society for Industrial and Applied Mathematics.

Green, C. C. 2015 Analytical solutions for two hollow vortex configurations in an infinite channel. *Eur. J. Mech. B/Fluids* **54**, 69–81.

Kamm, J. R. 1987 Shape and stability of two-dimensional uniform vorticity regions. PhD thesis, California Institute of Technology.

Kida, S. 1981 Motion of an elliptic vortex in a uniform shear flow. *J. Phys. Soc. Japan* **50**, 3517–3520.

Lamb, H. 1932 *Hydrodynamics*, sixth edn. Cambridge: Cambridge University Press.

Leppington, F. G. 2006 The field due to a pair of line vortices in a compressible fluid. *J. Fluid Mech.* **559**, 45–55.

Llewellyn Smith, S. G. & Crowdy, D. G. 2012 Structure and stability of hollow vortex equilibria. *J. Fluid Mech.* **691**, 178–200.

Luzzatto-Fegiz, P. & Williamson, C. H. K. 2011 An efficient and general numerical method to compute steady uniform vortices. *J. Comput. Phys.* **230**, 6495–6511.

Miyazaki, T., Imai, T. & Fukumoto, Y. 1995 Three-dimensional instability of Kirchhoff's elliptic vortex. *Phys. Fluids* **7**, 195–202.

Moore, D. W. & Pullin, D. I. 1987 The compressible vortex pair. *J. Fluid Mech.* **185**, 171–204.

Moore, D. W. & Saffman, P. G. 1971 Structure of a line vortex in an imposed strain. In *Aircraft wake turbulence and its detection* (ed. J. A. Olsen, A. Goldburg & M. Rogers), pp. 339–354. New York: Plenum.

Moore, D. W., Saffman, P. G. & Tanveer, S. 1988 The calculation of some Batchelor flows: The Sadovskii vortex and rotational corner flow. *Phys. Fluids* **31**, 978–990.

Overman, E. A. 1986 Steady-state solutions of the Euler equations in two dimensions II. Local analysis of limiting V-states. *SIAM J. Appl. Math.* **46**, 765–800.

Pocklington, H. C. 1895 The configuration of a pair of equal and opposite hollow straight vortices of finite cross-section, moving steadily through fluid. *Proc. Camb. Phil. Soc.* **8**, 178–187.

Robinson, A. C. & Saffman, P. G. 1984 Three-dimensional stability of an elliptical vortex in a straining field. *J. Fluid Mech.* **142**, 451–466.

Sadovskii, V. S. 1971 Vortex regions in a potential stream with a jump of Bernoulli's constant at the boundary. *App. Math. Mech.* **35**, 729–735.

Saffman, P. G. 1992 *Vortex dynamics*. Cambridge: Cambridge University Press.

Saffman, P. G. & Tanveer, S. 1982 The touching pair of equal and opposite uniform vortices. *Phys. Fluids* **25**, 1929–1930.

Saffman, P. G. & Tanveer, S. 1984 Prandtl–Batchelor flow past a flat plate with a forward-facing flap. *J. Fluid Mech.* **143**, 351–365.

Zabusky, N. J., Hughes, M. H. & Roberts, K. V. 1979 Contour dynamics for the Euler equations in two dimensions. *J. Comput. Phys.* **30**, 96–106.

Zannetti, L., Ferlauto, M. & Llewellyn Smith, S. G. 2016 Hollow vortices in shear. *J. Fluid Mech.* **809**, 705–715.